

Surface evolution of thermoelectric material KCu_4Se_3 explored by scanning tunneling microscopy

Yumin Xia(夏玉敏), Ni Ma(马妮), Desheng Cai(蔡德胜), Yuzhou Liu(刘宇舟), Yitong Gu(谷易通), Gan Yu(于淦), Siyu Huo(霍思宇), Wenhui Pang(庞文慧), Chong Xiao(肖翀), and Shengyong Qin(秦胜勇)
Citation: Chin. Phys. B, 2024, 33 (**8**): 086804. DOI: 10.1088/1674-1056/ad50c4

What follows is a list of articles you may be interested in

Growth and characterization of Bi(110)/$CrTe_2$ heterostructures: Exploring interplay between magnetism and topology

Zhenyu Yuan(袁震宇), Fazhi Yang(杨发枝), Baiqing Lv(吕佰晴), Yaobo Huang(黄耀波), Tian Qian(钱天), Jinpeng Xu(徐金朋), and Hong Ding(丁洪)
Chin. Phys. B, 2024, 33 (**2**): 026802. DOI: 10.1088/1674-1056/ad082a

Selective formation of ultrathin PbSe on Ag(111)

Jing Wang(王静), Meysam Bagheri Tagani, Li Zhang(张力), Yu Xia(夏雨), Qilong Wu(吴奇龙), Bo Li(黎博), Qiwei Tian(田麒玮), Yuan Tian(田园), Long-Jing Yin(殷隆晶), Lijie Zhang(张利杰), and Zhihui Qin(秦志辉)
Chin. Phys. B, 2022, 31 (**9**): 096801. DOI: 10.1088/1674-1056/ac7867

Realization of semiconducting Cu_2Se by direct selenization of Cu(111)

Yumu Yang(杨雨沐), Qilong Wu(吴奇龙), Jiaqi Deng(邓嘉琦), Jing Wang(王静), Yu Xia(夏雨), Xiaoshuai Fu(富晓帅), Qiwei Tian(田麒玮), Li Zhang(张力), Long-Jing Yin(殷隆晶), Yuan Tian(田园), Sheng-Yi Xie(谢声意), Lijie Zhang(张利杰), and Zhihui Qin(秦志辉)
Chin. Phys. B, 2021, 30 (**11**): 116802. DOI: 10.1088/1674-1056/ac0037

Covalent coupling of DNA bases with graphene nanoribbon electrodes: Negative differential resistance, rectifying, and thermoelectric performance

Peng-Peng Zhang(张鹏鹏), Shi-Hua Tan(谭仕华)†, Xiao-Fang Peng(彭小芳)‡, and Meng-Qiu Long(龙孟秋)
Chin. Phys. B, 2020, 29 (**10**): 106801. DOI: 10.1088/1674-1056/aba9bf、

Thermoelectric properties of two-dimensional hexagonal indium-VA

Jing-Yun Bi(毕京云), Li-Hong Han(韩利红), Qian Wang(王倩), Li-Yuan Wu(伍力源), Ruge Quhe(屈贺如歌), Peng-Fei Lu(芦鹏飞)
Chin. Phys. B, 2018, 27 (**2**): 026802. DOI: 10.1088/1674-1056/27/2/026802

Surface evolution of thermoelectric material KCu_4Se_3 explored by scanning tunneling microscopy

Yumin Xia(夏玉敏)[1,2], Ni Ma(马妮)[3,4], Desheng Cai(蔡德胜)[1,2], Yuzhou Liu(刘宇舟)[1,2], Yitong Gu(谷易通)[1,2], Gan Yu(于淦)[1,2], Siyu Huo(霍思宇)[1,2], Wenhui Pang(庞文慧)[1,2], Chong Xiao(肖翀)[3,4,5], and Shengyong Qin(秦胜勇)[1,2,6,†]

[1] *International Center for Quantum Design of Functional Materials (ICQD), Hefei National Laboratory for Physical Sciences at Microscale (HFNL), University of Science and Technology of China, Hefei* 230026, *China*

[2] *CAS Key Laboratory of Strong Coupled Quantum Matter Physics, Department of Physics, University of Science and Technology of China, Hefei* 230026, *China*

[3] *Hefei National Laboratory for Physical Sciences at the Microscale, University of Science and Technology of China, Hefei* 230026, *China*

[4] *Institute of Energy, Hefei Comprehensive National Science Center, Hefei* 230031, *China*

[5] *Dalian National Laboratory for Clean Energy, Chinese Academy of Sciences (CAS), Dalian* 116023, *China*

[6] *Hefei National Laboratory, University of Science and Technology of China, Hefei* 230088, *China*

(Received 10 May 2024; revised manuscript received 27 May 2024; accepted manuscript online 28 May 2024)

Novel two-dimensional thermoelectric materials have attracted significant attention in the field of thermoelectric due to their low lattice thermal conductivity. A comprehensive understanding of their microscopic structures is crucial for driving further the optimization of materials properties and developing novel functional materials. Here, by using *in situ* scanning tunneling microscopy, we report the atomic layer evolution and surface reconstruction on the cleaved thermoelectric material KCu_4Se_3 for the first time. We clearly revealed each atomic layer, including the naturally cleaved K atomic layer, the intermediate Se^{2-} atomic layer, and the Se^{-} atomic layer that emerges in the thermodynamic-stable state. Departing from the majority of studies that predominantly concentrate on macroscopic measurements of the charge transport, our results reveal the coexistence of potassium disorder and complex reconstructed patterns of selenium, which potentially influences charge carrier and lattice dynamics. These results provide direct insight into the surface microstructures and evolution of KCu_4Se_3, and shed useful light on designing functional materials with superior performance.

Keywords: thermoelectric, KCu_4Se_3, scanning tunneling microscopy (STM), evolution

PACS: 68.60.Dv, 72.15.Jf, 73.25.+i **DOI:** 10.1088/1674-1056/ad50c4

1. Introduction

Two-dimensional (2D) thermoelectric materials distinguish themselves through the distinct chemical bonding within the family of thermoelectric materials.[1–6] The hierarchical structure with strong intralayer and weak interlayer interaction[7] endows an ideal platform for tuning the transport properties.[8–12] Therefore, the microscopic understanding of structure for these functional materials is of great significance, not only for the community of thermoelectricity but also the solid chemistry and materials science. For instance, the electrical conductivity of monolayer MoS_2 significantly exceeds that of its bulk counterpart, demonstrating considerable tunability of its Seebeck coefficient under an external electric field.[13–15] Regarding the phonon heat in SnSe, the Sn lone pair electrons act as a driving force for the large anharmonicity, resulting in the low lattice thermal conductivity.[16–19] Additionally, in the typical thermoelectric materials Cu_2Se,[20,21] the suppression of transverse phonon modes primarily arises from the highly disordered Cu ions.[22,23]

The class of transition-metal chalcogenides, A/Cu/Q (A = alkali metal, Q = chalcogen)[24–27] has been of continuing interest over the years due to its complex structure and compositional diversity.[28–32] These materials show the potential for large lattice anharmonicity, such as the large phonon anharmonicity in $CsCu_4Se_3$ stems from the hierarchy of the rigid $[(Cu^{+})_4(Se^{2-})_2](Se^{-})$ double anti-CaF_2 layer and the soft Cs^{+} sublattice,[33] resulting in a lower phonon frequency than Cu_2Se.[20] It is worth noting that the current research on these materials predominantly focuses on the theoretical calculations and macroscopic characterization. Therefore, the observation of microscopic details holds crucial significance, which may gain new atomistic-level insights into the conduction physics.

Herein, we employ *in situ* scanning tunneling microscopy (STM) to investigate the surface structure and its thermally driven evolution in KCu_4Se_3. By combined the measurement of the spacing between different atomic layers with observation of the KCu_4Se_3 surface structure evolution during annealing, we reveal the transition from the naturally cleaved K atomic layer, through the emergence of the intermediate Se^{2-} atomic layer, to the stable-state Se^{-} atomic layer. Concurrently, the Se^{2-} and Se^{-} layers undergo a relaxation pro-

†Corresponding author. E-mail: syqin@ustc.edu.cn

© 2024 Chinese Physical Society and IOP Publishing Ltd

cess from their intrinsic lattice structures, evolving into complex reconstructed patterns, as illustrated by our simulations. Our exploration into the microstructure and evolution of 2D thermoelectric materials offers an intuitive insight, laying the foundation for innovative materials preparation strategies and enhanced properties.

2. Experiment

2.1. Crystals preparation

Reagents of amorphous B powders (99.99%), K_2CO_3 powders (99.99%), Cu powders (99.999%), and Se powders (99.999%) were used as purchased from Alfa Aesar. The synthesis procedure was inspired by the boron–chalcogen method,[28,29,33] plenty of shining KCu_4Se_3 crystals were obtained by melting K_2CO_3, Cu, B, and Se with stoichiometric ratio of K_2CO_3/Cu/B/Se = 3/24/2/18 at 973 K for 3 h then slowly cooled to room temperature.

2.2. STM measurements

The KCu_4Se_3 sample was cleaved in the preparation chamber with a base pressure of 2.0×10^{-10} Torr (1 Torr = 1.33322×10^2 Pa) at 90 K and immediately transferred into the STM scan head. The STM stage was kept at 78 K throughout the measurements, while the annealing process was performed at room temperature. Our experiments were performed *in situ* in a Unisoku 1500 STM system with the RHK R9 controller. All STM topographic images were obtained in a constant current mode with the bias voltage V applied to the sample. A standard lock-in technique was used for the STS measurements with a small bias modulation of 5 mV at 1.699 kHz. Image extraction and data analysis were performed in the latest version of WsXM.[34]

3. Results and discussion

Bulk KCu_4Se_3 is in the shape of flakes after stripped from the reaction tube and crystal itself is mostly flat, except at the edges, which indicates relatively rare crystal intergrowth. The crystal is not particularly air-sensitive and can be easily cleaved due to its layer structure nature. Figure 1(a) shows the typical large-scale STM topography of the cleaved surface with the flat terrace and sharp steps. The corresponding atomic image presented in Fig. 1(b), reveals a tetragonal atomic structure marked with the blue dots. The distance between the adjacent bright atoms, measured at 4.11 Å, is analyzed from the line profile in Fig. 1(c). Given that the theoretical lattice constants for both the K and Se atomic planes are 0.40 nm,[33] the cleaved plane remains uncertain from the lattice structure alone, which will be the subject of detailed analysis and discussion later. Figure 1(d) presents the line profile of the step height for the cleaved surface, aligning with the 0.98-nm theoretical height of a KCu_4Se_3 monolayer. In addition, the cross-step $\mathrm{d}I/\mathrm{d}V$ line spectra depicted in Fig. 1(e) demonstrate uniformity of the surface electronic states within a wide sample bias range (1.5 V to +1.5 V), signifying the high quality of the KCu_4Se_3 sample. Significantly, the $\mathrm{d}I/\mathrm{d}V$ spectrum measurement conducted over a narrow bias range, as illustrated in Fig. 1(f), further confirms that KCu_4Se_3 is heavily electron-poor,[33] with the lowest density of states (DOS) located at approximately −0.68 eV. This characteristic likely results from fabricating the sample in an Se-rich environment.

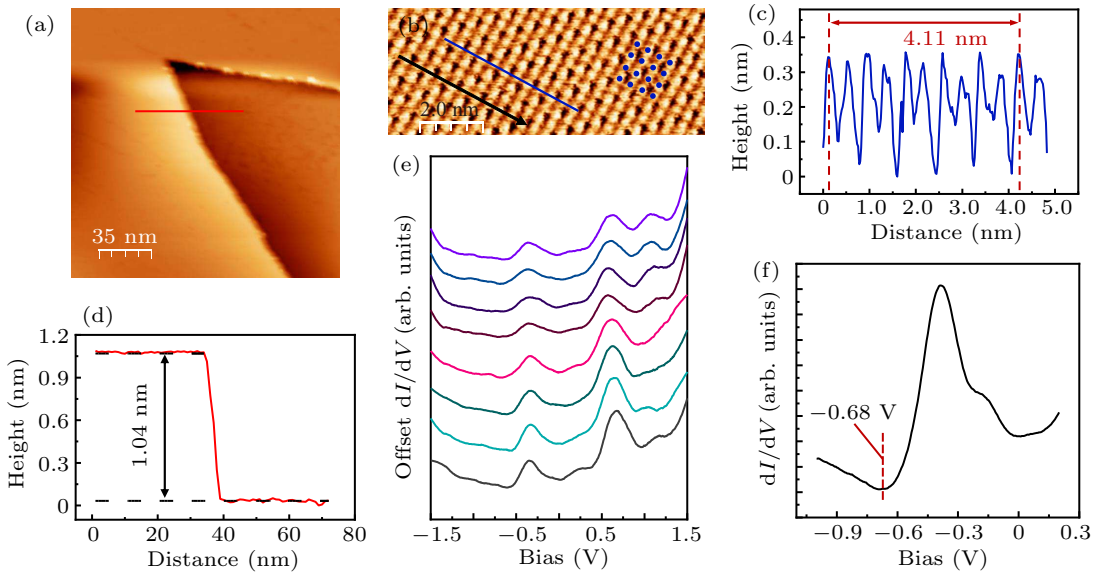


Fig. 1. STM topography images of crystal and $\mathrm{d}I/\mathrm{d}V$ spectra of a naturally cleaved surface. (a) Large-area topography (125 nm×125 nm, $V = 2.0$ V, and $I = 10$ pA) with the terraces. (b) Atomic structure of cleaved surface of KCu_4Se_3 (10 nm×4 nm, $V = 60$ mV, and $I = 150$ pA) and (c) the lattice constant. (d) Height profile measured along the red solid line marked in panel (a). (e) The cross-step $\mathrm{d}I/\mathrm{d}V$ line spectra, which are shifted vertically for clarity. (f) $\mathrm{d}I/\mathrm{d}V$ spectrum over a narrow voltage range.

Upon annealing the cleaved KCu_4Se_3 sample at room temperature in an ultra-high vacuum, intriguing changes are observed on the sample's surface. Figure 2(a) shows the large-scale STM surface topography of KCu_4Se_3, annealed at room temperature for 2 hours after natural cleavage. We observed that the surface morphology of the KCu_4Se_3 involves significant transformations during the annealing process, with the previously uniform and clean surface evolving into one exposing two terminations. Figures 2(b) and 2(c) display enlarged, detailed topography images of two different terminal surface corresponding to the green and purple boxes in Fig. 2(a), respectively. For clarity in subsequent discussions, we will name the higher terminal as surface I and the lower as surface II. Although the surface I retains aspects of its pre-annealed morphology, it now exhibits numerous new defects, including large circular bright spots, dark atom-deficient point defects, and dimers-like atoms with no obvious preferred orientation, as outlined within the green circles in Fig. 2(b). Meanwhile, surface II shows a relatively more orderly arrangement of one-dimensional (1D) periodic atomic chains with uniformly attached atoms, indicated by the purple circle in Fig. 2(c). The relative height between surface I and surface II presented in Fig. 2(d) measures approximately 1.6 Å, corresponding to the solid red line in Fig. 2(a).

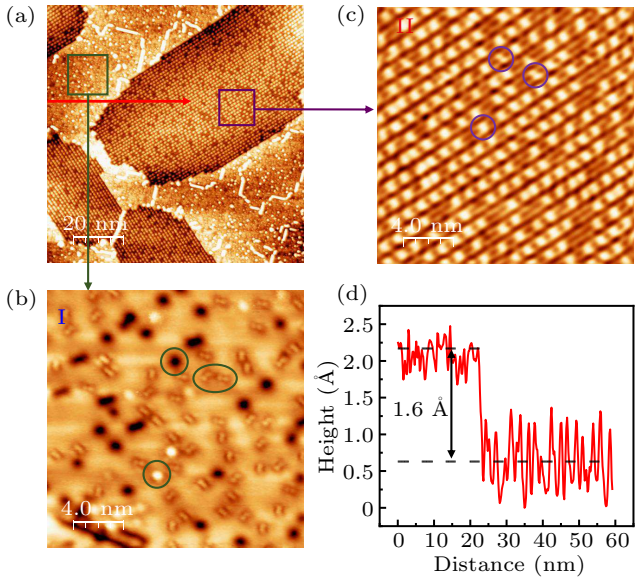


Fig. 2. Typical STM topography images of the KCu_4Se_3 surface annealed at room temperature for 2 hours. (a) Large-area surface topography (100 nm×100 nm, $V = 1.0$ V, and $I = 10$ pA) of two atomic layers (surfaces I and II), as shown by the square marked in green and purple. (b)–(c) Zoom in images of the two areas (20 nm×20 nm, (b) $V = 0.5$ V and $I = 35$ pA, (c) $V = 0.4$ V and $I = 110$ pA), as shown by the arrows of the corresponding colors. (d) Height profile taken along the red line as marked in panel (a).

With further annealing, the surface topography of KCu_4Se_3 undergoes continuous transformation. Figures 3(a) and 3(b) show the typical large-scale STM surface topography image and corresponding detailed topography after 5 days of annealing. Compared with the previous stage, the surface I is preserved, while the coverage of surface II characterized by 1D atomic chains substantially increases. These chains are aligned perpendicularly to one another and vary randomly in single, double, or triple rows. Simultaneously, a third surface emerges, named terminal surface III and highlighted by a green mark in Fig. 3. The newly revealed surface III appears to have been shaped by a vigorous and intricate molecular dynamic process, primarily consisting of linearly arranged atomic groups and sophisticated triangular reconstruction patterns. Furthermore, topography observation reveals that naturally cleaved KCu_4Se_3 not only displays different atomic planes on its uppermost layer (including surfaces, I, II, and III), but also exposes the atomic surface of the subtop layer progressively during further annealing processes. STM measurements of the relative heights of these specific atomic surfaces presented in Fig. 3(c), demonstrate a height differential of $h_{12} = 2.0$ Å between surfaces I and II, $h_{2-1} = 7.7$ Å between surface II and the corresponding surface I of the succeeding unit cell, and $h_{23} = 3.1$ Å between surfaces II and III. Compared to the surface II exposed at the initial annealing stage, the height difference between surfaces I and II in this stage more closely matches the true height of 2.0 Å. This may be attributed to the initial presence of mobile K atoms on surface II. Furthermore, through further annealing, the morphological structure of surface II has evolved from a transitional state to the reconstructed surface observed currently. Following a third round of room temperature annealing, the surface topography of the KCu_4Se_3 sample finally stabilizes, transitioning from a previously complex and varied surfaces state to a clearer configuration characterized by the alternating appearances of surfaces I and III, as illustrated in Figs. 3(d) and 3(e). The coverage of surface III significantly increases compared to the previous stage, either being surrounded by surface I within the same unit cell or aligned along the step edges thereby connecting to surface I of the subsequent unit cell. In both scenarios, the edges connecting surfaces I and III lack a relative preferred distribution, indicating a completely random movement of surface atoms. Concurrently, measurements of the relative height difference between surfaces in this phase of stabilization were undertaken, as shown in Fig. 3(f). The heights differential between surfaces I and III are measured to be $h_{13} = 4.8$ Å and 4.85 Å, and the height difference from the surface III to surface I of next unit cell is determined to be $h_{3-1} = 4.9$ Å. It is noteworthy that the surface topographies presented herein are derived form an extensive dataset, achieved by varying the sample areas and different samples to mitigate the influence of randomness and localized anomalies as much as possible. Additionally, the height results are aggregated through statistical methods, ensuring the minimization of errors attributable to the measurement process.

Accordingly, we can analyze the surface evolution pro-

cess of KCu_4Se_3 though the different annealing stages, driving purely by thermal. As mentioned above, despite the K atomic layer and the Se^{2-} atomic layer are interconnected by the weak van der Waals forces, their top view lattice parameters aligned (differing only in relative angle) and the densities of electronic state show similar. Therefore, we cannot ascertain the cleaved surface from the STM images following natural mechanical exfoliation. For the intermedia states (Figs. 3(a) and 3(b)), where surfaces I, II, and III are continuously distributed, a complete unit cell period can be considered extending from surface I to its successive iteration in the next unit cell. Height measurements presented in Fig. 3(c) reveal that the height difference between surface III and surface I of the next unit cell is $h_{3-1} = 4.6$ Å ($h_{3-1} = h_{2-1} - h_{23}$), which is basically consistent with the measurement results in Fig. 3(f) of the stable states (Figs. 3(d) and 3(e)). We propose a possible model to describe the evolution of surface topography throughout stages of the annealing process. Figures 4(a)–4(c) display the simulated surface topographies of KCu_4Se_3, depicting the freshly cleaved, annealed intermediate, and final stable states, respectively. Figure 4(d) offers a lateral view of the lattice structure, with the relative heights between atomic layers annotated on the left.

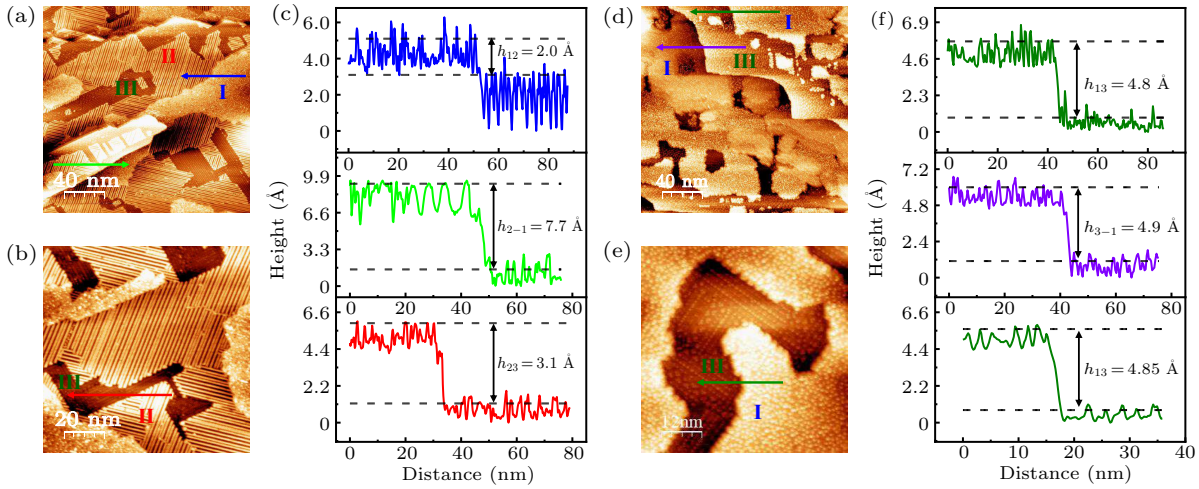


Fig. 3. Typical STM topography images of the KCu_4Se_3 surfaces annealed for 5 days and 20 days. Different surfaces are indicated by areas I, II, and III marked blue, red, and green respectively. Corresponding colors and numbers in images indicate the same surface types. (a) Large-area topographies displaying surfaces I, II, and III (200 nm×200 nm, $V = 2.0$ V, and $I = 5$ pA). (b) Zoom-in image of the surface annealed for 5 days (100 nm×100 nm, $V = 1.5$ V, and $I = 10$ pA). (c) Height profile of color lines in panels (a) and (b). (d) Large-area topographies displaying surfaces I and III (200 nm×200 nm, $V = 1.0$ V, and $I = 10$ pA). (e) Zoom-in images of the surface annealed for 20 days (60 nm×60 nm, $V = 2.5$ V, and $I = 25$ pA). (f) Height profile of color lines in panels (d) and (e). The arrow indicates the measurement direction.

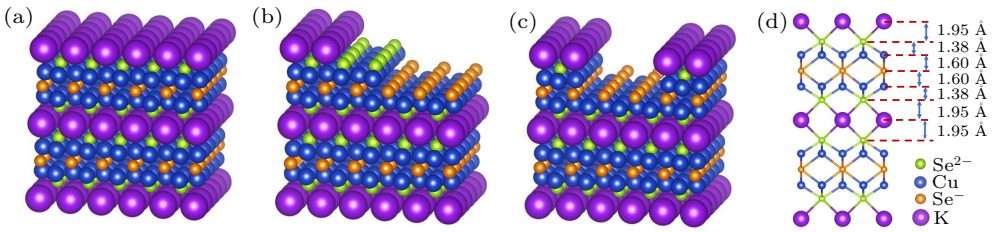


Fig. 4. Simulation diagram depicting the evolution of the KCu_4Se_3 surface as observed by STM throughout the annealing process. (a) Fresh naturally cleaved surface topography, (b) surface after 5 days, (c) surface after 20 days. (d) Side-view of the KCu_4Se_3 lattice structure, annotated with the spacing between the individual atomic layers.

Initially, we assume that the comparatively disordered surface I serves as the natural cleavage plane, attributed to the K atomic layer. During the early annealing phase, K atoms on the topmost surface I begin to migrate across the surface, driven by the thermal energy, which is consistent with the high mobility of K atoms.[35,36] As the annealing progress, the subsequent atomic layer (surface II) becomes exposed. This layer shows a height difference of 2.0 Å, identifying it as corresponding to Se^{2-} atomic layer. Continuing the annealing process unveils surface III with a height difference of $h_{23} = 3.1$ Å, indicating its correspondence to the Se^{-} surface. Notably, the height between surface III and surface I of the adjacent unit cell ($h_{3-1} = 4.6$ Å), represents the separation between the Se^{-} atomic layer (surface III) and the K atomic layer (surface I) of the succeeding cell. This observation aligns well with the height difference of $h_{3-1} = 4.9$ Å observed in the final state. To rule out alternative hypotheses and further substantiate our conclusion, we consider a scenario wherein the naturally cleaved surface corresponds to the Se^{2-} atomic layer (surface I). Integrating this with the height results among the

atomic layers, we find that surface III in the final stable state, characterized by a height difference (h_{13}) of 4.8 Å, should correspond to the Cu atomic layer. In the intermediary stage, where surfaces I, II, and III are simultaneously exposed, the height differences are recorded as: $h_{12} = 2.0$ Å, $h_{23} = 3.1$ Å, and $h_{2-1} = 7.7$ Å. This configuration suggests that surface II aligns with the Se^{-} atomic layer, and surface III with the Se^{2-} atomic layer. Nevertheless, the scenario proves to be untenable. It is important to note that to ensure the accuracy of our measurements, the height differences between atomic layer planes are determined by scanning multiple samples and areas.

To investigate the surface reconstruction of KCu_4Se_3, we concentrate on analyzing the topographical characteristics of the Se^{2-} (surface II) and Se^{-} (surface III) atomic layer as revealed by annealing. Notably, the second annealing stage unveils approximately 60% exposure of the Se^{2-} atomic layer, predominantly featuring two perpendicularly oriented 1D atomic chains. Figure 5(a) displays a typical reconstruction of the Se^{2-} atomic layer, showcasing atomic chains primarily in pairs with alternating bright and dark aggregations along with double or triple chains. The spacing between adjacent bright atomic chains measures approximately 2.1 nm, with the spacing between individual bright spots of these chains being 0.56 nm. This 2.1-nm spacing corresponds to $4\sqrt{2}$ times the lattice constants ($a = b = 0.4$ nm) of the Se^{2-} layer, closely matching the theoretical value of 2.24 nm. Likewise, the 0.56-nm spacing of the bright (dark) spots is $\sqrt{2}$ times the lattice constant, consistent with theoretical value. A simplified simulation diagram depicted in Fig. 5(b), illustrates the atomic reconfiguration post-annealing relaxation. Here, the blue box on the left outlines the lattice of the Se^{2-} atomic layer, the red box indicates the reconfigured lattice to $\sqrt{2}$ times its original size, and the red stripes are the bright atomic chains formed by the aggregation of bright spots. In the third stable state, the coverage of the Se^{-} atomic layer (surface III) significantly expands. Apart from symmetrically arranged triangular patterns, a 1D stripe pattern with alternating bright and dark spots is observed, as shown in Fig. 5(c). The bright and dark spots alternate with a spacing of 1.68 nm, while the distance between spots within a single stripe measures 1.14 nm. However, across many scanned topographies, the signal from the dark spot fringes is relatively weaker or even absent. The periodic spacing between the bright and dark atomic stripes is approximately four times the lattice spacing of the Se^{-} layer, with the spacing between adjacent light (dark) spots approximately three times the lattice spacing, as depicted in Fig. 5(d). Within this diagram, dark red and bright red represent the central Se atomic clusters within the bright and dark atomic chains, respectively. This lattice inhomogeneity and surface reconfiguration may significantly impact the system's electron–phonon interaction and charge transport behavior.[31,37]

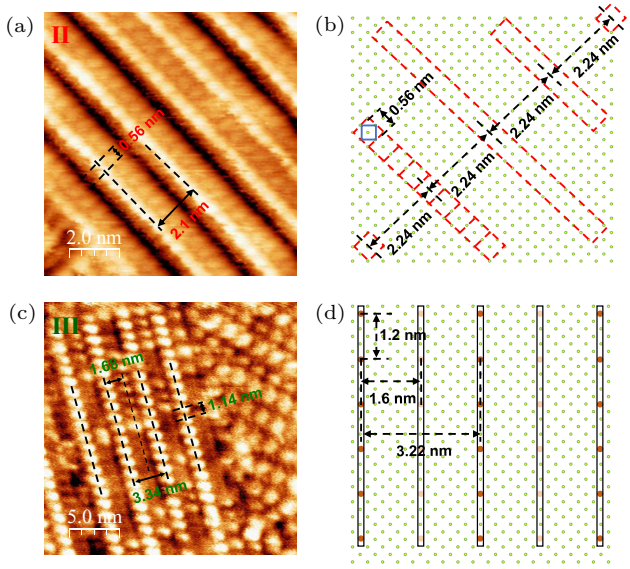


Fig. 5. The typical reconstruction topographies and corresponding simulation diagrams for (a), (b) (10 nm×10 nm, $V = 0.5$ V, and $I = 50$ pA) surface II and (c), (d) (25 nm×25 nm, $V = 0.5$ V, and $I = 50$ pA) surface III.

4. Conclusion

In summary, by using *in situ* STM, our study has provided valuable insight into the surface structural evolution of KCu_4Se_3 under thermal conditions. We have successfully observed the transitions between the K, Se^{2-}, and Se^{-} atomic layers, providing a clearer picture of the surface dynamics at the atomic level for the first time. The coexistence of potassium disorder and complex selenium reconstructed patterns may potentially affect charge carrier and lattice dynamics. These preliminary findings enhance our understanding microstructural behaviors in KCu_4Se_3 and offer potential pathways for optimizing material properties through surface engineering. Further investigations are needed to elucidate the kinetic and thermodynamic process involved, which could enable more precise control over the material properties for improved thermoelectric performance.

Acknowledgements

Project supported by the National Natural Science Foundation of China (Grant Nos. 12374196, 92165201, 11634011, and 22109153), the Innovation Program for Quantum Science and Technology (Grant No. 2021ZD0302800), the CAS Project for Young Scientists in Basic Research (Grant No. YSBR-046), the Fundamental Research Funds for the Central Universities (Grant Nos. WK3510000006 and WK3430000003), the Fund of Anhui Initiative in Quantum Information Technologies (Grant No. AHY170000), the University Synergy Innovation Program of Anhui Province, China (Grant No. GXXT-2022-008), and the National Synchrotron

Radiation Laboratory Joint Funds of University of Science and Technology of China (Grant No. KY2060000241).

References

[1] Biswas K, He J Q, Blum I D, Wu C I, Hogan T P, Seidman D N, Dravid V P and Kanatzidis M G 2012 *Nature* **489** 414

[2] Tan G J, Shi F Y, Hao S Q, Zhao L D, Chi H, Zhang X M, Uher C, Wolverton C, Dravid V P and Kanatzidis M G 2016 *Nat. Commun.* **7** 12167

[3] Jin Q, Jiang S, Zhao Y, Wang D, Qiu J, Tang D M, Tan J, Sun D M, Hou P X, Chen X Q, Tai K, Gao N, Liu C, Cheng H M and Jiang X 2018 *Nat. Mater.* **18** 62

[4] Acharyya P, Roychowdhury S, Samanta M and Biswas K 2020 *J. Am. Chem. Soc.* **142** 20502

[5] Slade T J, Pal K, Grovogui J A, Bailey T P, Male J, Khoury J F, Zhou X, Chung D Y, Snyder G J, Uher C, Dravid V P, Wolverton C and Kanatzidis M G 2020 *J. Am. Chem. Soc.* **142** 12524

[6] Zhou C, Yu Y, Lee Y L, Ge B, Lu W, Oana C M, Im J, Cho S P, Wuttig M, Shi Z and Chung I 2020 *J. Am. Chem. Soc.* **142** 15172

[7] Ma N, Xiao C and Xie Y 2024 *Acc. Mater. Res.* **5** 286

[8] Zhang J W, Song L R, Madsen G K H, Fischer K F F, Zhang W Q, Shi X and Iversen B B 2016 *Nat. Commun.* **7** 10892

[9] Liu Y C, Wang W X, Yang J and Li S 2018 *Adv. Sustain. Syst.* **2** 1800046

[10] Samanta M, Ghosh T, Chandra S and Biswas K 2020 *J. Mater. Chem. A* **8** 12226

[11] Chung D Y, Hogan T, Brazis P, Melissa R L, Kannewurf C, Bastea M, Uher C and Kanatzidis M G 2000 *Science* **287** 1024

[12] Li X Y, Bai W, Gao J Q, Li P J, Zhang R X, Xie K, Xia Y M, Shi H H, Xiao C, Xie Y and Qin S Y 2021 *J. Phys. Chem. Lett.* **12** 5319

[13] Li L K, Yu Y J, Ye G J, Ge Q Q, Ou X D, Wu H, Feng D L, Chen X H and Zhang Y B 2014 *Nat. Nanotechnol.* **9** 372

[14] Flores E, Ares J R, Castellanos-Gomez A, Barawi M, Ferrer I J and Sánchez C 2015 *Appl. Phys. Lett.* **106** 022102

[15] Lv H Y, Lu W J, Shao D F and Sun Y P 2014 *Phys. Rev. B* **90** 085433

[16] Zhao L D, Lo S H, Zhang Y, Sun H, Tan G, Uher C, Wolverton C, Dravid V P and Kanatzidis M G 2014 *Nature* **508** 373

[17] Zhao L D, Tan G J, Hao S Q, He J Q, Pei Y L, Chi H, Wang H, Gong S K, Xu H B, Dravid V P, Uher C, Snyder G J, Wolverton C and Kanatzidis M G 2016 *Science* **315** 141

[18] Duong A T, Nguyen V Q, Duvjir G, Duong V T, Kwon S, Song J Y, Lee J K, Lee J E, Park S, Min T, Lee J, Kim J and Cho S 2016 *Nat. Commun.* **7** 13713

[19] Chang C, Wu M H, He D S, Pei Y L, Wu C F, Wu X F, Yu H L, Zhu F Y, Wang K D, Chen Y, Huang L, Li J F, He J Q and Zhao L D 2018 *Science* **360** 778

[20] Liu H L, Shi X, Xu F F, Zhang L L, Zhang W Q, Chen L D, Li Q, Uher C, Day T and Snyder G J 2012 *Nat. Mater.* **11** 422

[21] Bai H, Su X L, Yang D W, Zhang Q J, Tan G J, Uher C, Tang X F and Wu J S 2021 *Adv. Funct. Mater.* **31** 2100431

[22] Qian K, Gao L, Chen X, Li H, Zhang S, Zhang X L, Zhu S, Yan J, Bao D, Cao L, Shi J A, Lu J, Liu C, Wang J, Qian T, Ding H, Gu L, Zhou W, Zhang Y Y, Lin X, Du S, Ouyang M, Pantelides S T and Gao H J 2020 *Adv. Mater.* **32** 1908314

[23] Gulay L, Daszkiewicz M, Strok O and Pietraszko A 2011 *Chem. Met. Alloys* **4** 200

[24] Folmer J C W and Jellinek F 1980 *J. Less-Common Met.* **76** 153

[25] Stoll P, Näther C, Jeß I and Bensch W 1999 *Acta Cryst.* **C55** 286

[26] Klepp K, Boller H and Völlenkle H 1980 *Monatshefte für Chemie/Chemical Monthly* **111** 727

[27] McKeever H, Patil N N, Palabathuni M and Singh S 2023 *Chem. Mater.* **35** 9833

[28] Ma N, Jia F, Xiong L, Chen L, Li Y Y and Wu L M 2019 *Inorg Chem.* **58** 1371

[29] Ma N, Li Y Y, Chen L and Wu L M 2020 *J. Am. Chem. Soc.* **142** 5293

[30] Chen Y Y, Shen Y P, Li X Y, Sun J and Wang Q 2020 *Adv. Theory Simul.* **3** 2000169

[31] Chen H J, Rodrigues J N B, Rettie A J E, Song T B, Chica D G, Su X L, Bao J K, Chung D Y, Kwok W K, Wagner L K and Kanatzidis M G 2019 *J. Am. Chem. Soc.* **141** 635

[32] Sturza M, Malliakas C D, Bugaris D E, Han F, Chung D Y and Kanatzidis M G 2014 *Inorg. Chem.* **53** 12191

[33] Ma N, Li F, Li J G, Liu X, Zhang D B, Li Y Y, Chen L and Wu L M 2021 *J. Am. Chem. Soc.* **143** 18490

[34] Horcas I, Fernandez R, Gomez-Rodriguez J M, Colchero J, Gomez-Herrero J and Baro A M 2007 *Rev. Sci. Instrum.* **78** 013705

[35] Yin F, Akola J, Koskinen P, Manninen M and Palmer R E 2009 *Phys. Rev. Lett.* **102** 106102

[36] Renard J, Lundeberg M B, Folk J A and Pennec Y 2011 *Phys. Rev. Lett.* **106** 156101

[37] Zhou J J, Hellman O and Bernardi M 2018 *Phys. Rev. Lett.* **121** 226603